ADVANCED
FUNCTIONAL
MATERIALS

Bulk Incorporation of Molecular Dopants into Ruddlesden–Popper Organic Metal–Halide Perovskites for Charge Transfer Doping

Jonghoon Lee, Kyeong-Yoon Baek, Jeongjae Lee, Heebeom Ahn, Yongjin Kim, Hyungbin Lim, Yeeun Kim, Jaeyong Woo, Samuel D. Stranks, Sung Keun Lee, Henning Sirringhaus, Keehoon Kang,* and Takhee Lee*

Organic metal-halide perovskites (OHPs) have recently attracted much attention as next-generation semiconducting materials due to their outstanding opto-electrical properties. However, OHPs currently suffer from the lack of efficient doping methods, while the traditional method of atomistic doping having clear limitations in the achievable doping range. While doping with molecular dopants, has been suggested as a solution to this problem, the action of these dopants is typically restricted to perovskite surfaces, therefore significantly reducing their doping potential. In this study, successful bulk inclusion of "magic blue", a molecular dopant, into 2D Ruddlesden–Popper perovskites is reported. This doping strategy of immersing the perovskite film in dopant solution increases the electrical current up to ≈60 times while maintaining clean film surface. A full mechanistic picture of such immersion doping is provided, in which the solvent molecule facilitates bulk diffusion of dopant molecule inside the organic spacer layer. Physical criteria for judicious choice of solvents in immersion doping are developed based on readily available solvent properties. The immersion doping method developed in this study that enables bulk molecular doping in OHPs will provide a strategic doping methodology for controlling electrical properties of OHPs for electronic and optoelectronic devices.

1. Introduction

Organic metal-halide perovskites (OHPs) have received much spotlight as next-generation semiconductor materials due to a number of advantages such as facile solution processing[1] and defect tolerance.[2] Despite these advantages, perovskite-based semiconductors lack the controllability in their electrical properties, especially their conductivity and Fermi level via doping,[3] which set crucial challenges that need to be overcome to see their adoption in high-performance optoelectronic[1a,4–6] and electronic devices.[1b,c,7,8]

Doping research in perovskites has been mainly focused on defect passivation via atomic substitution with non-stoichiometric impurities[9] for improving the device efficiency of solar cells[10] and light emitting diodes[11] by suppressing non-radiative recombination in the active perovskite layer.[10b,11,12] Such substitutional doping with heterovalent atomic dopants (e.g., Sb,[13] Bi,[14] Li,[15] Ag,[16] and Na[17]), although well-established in traditional semiconductor materials such as silicon, is limited due to the constraints on

J. Lee, K.-Y. Baek, H. Ahn, H. Lim, Y. Kim, J. Woo, T. Lee
Department of Physics and Astronomy, and Institute of Applied Physics
Seoul National University
08826 Seoul, South Korea
E-mail: tlee@snu.ac.kr

J. Lee, S. K. Lee
School of Earth and Environmental Sciences
Seoul National University
08826 Seoul, South Korea

Y. Kim, K. Kang
Department of Materials Science and Engineering
Seoul National University
08826 Seoul, South Korea
E-mail: keehoon.kang@snu.ac.kr

S. D. Stranks, H. Sirringhaus
Optoelectronics Group
Department of Physics
Cavendish Laboratory
University of Cambridge
CB3 0HE Cambridge, UK

S. K. Lee, K. Kang
Institute of Applied Physics
Seoul National University
08826 Seoul, South Korea

K. Kang
Research Institute of Advanced Materials
Seoul National University
08826 Seoul, South Korea

2302048 (1 of 11)

**ADVANCED
SCIENCE NEWS**

www.advancedsciencenews.com

**ADVANCED
FUNCTIONAL
MATERIALS**

www.afm-journal.de

the suitable atomic sizes for replacing A, B, and X sites in OHPs (as a form of ABX_3). This is because in general, substitutional doping in metal halide perovskites is performed at much higher concentrations (0.5–10%)[13–17] than ppm–ppt level as commonly performed in conventional silicon-based semiconductors; structural stability at such high concentration is mainly determined by ionic sizes in forms of, for example, Goldschmidt tolerance factor.[18] In addition, even if a dopant atom can be incorporated into the perovskite structure, there is a limit to the tunability range of electrical conductivity values that can be achieved with substitutional doping due to the compositional range allowed by the tolerance factor.

On the other hand, organic molecules offer ample space for versatility and tunability of molecular structures and functional groups. Doping with organic molecules has been a successful strategy widely adopted in organic electronics field, where enhancements over several orders of magnitudes in electrical conductivities are common.[19] While similar attempts on molecular doping of perovskites with 2,3,5,6-tetrafluoro-tetracyanoquinodimethane (F_4TCNQ),[19b,20] $C_{24}H_{22}N_2^{2+}$ (benzyl viologen, denoted as BV)[21] and [Co(η_5-C_5H_5)$_2$] (cobaltocene)[22] have been reported previously, these works relied on charge transfer between the perovskite *surface* and molecular dopants ("surface doping") as the primary mechanism of doping. The drawbacks of such surface doping are obvious: the superficial nature of interaction poses a limit on the level of achievable carrier concentration and mobility,[20,22b] as well as making the dopants more prone to surface-initiated degradation.[22b] In contrast, charge transfer by incorporation of molecular dopants into the bulk perovskite structure[23] ("bulk doping") would be a promising route to solve both of these problems inherent to surface doping strategies if sufficiently large free spaces are made available within the perovskite lattice.

2D perovskites, a group of recently highlighted perovskite derivatives with organic spacer ions between the perovskite layers, provide an ideal system for meeting this requirement. Following this route, we hereby demonstrate a successful solvent-assisted incorporation of tris(4-bromophenyl)ammoniumyl hexachloroantimonate ([(4-BrC_6H_4)$_3$N]$SbCl_6$),[24] a widely used molecular dopant also known as "magic blue", within the 2D butylammonium lead iodide (BA_2PbI_4) perovskite structure through an immersion doping strategy. Solid-state nuclear magnetic resonance (NMR) measurements on the doped sample reveal bulk incorporation of magic blue molecules within the organic layer of perovskite structure, which subsequently results in ≈60-fold enhancement in electrical conductivity. A set of criteria for selecting the dopant/solvent pair in the immersion doping approach is developed in terms of dopant/solvent physical properties. Extensions of this idea to other (n ≥ 2) 2D lead iodide perovskites are also discussed.

2. Results and Discussion

2.1. Structure and Doping of Low-Dimensional 2D RP Perovskites

Ruddlesden–Popper (RP) perovskites originally belong to a family of low-dimensional perovskites with alternating perovskite- and rocksalt-like layers.[25] In the context of organic–inorganic hybrid perovskite, however, they almost exclusively refer to a class of 2D perovskites with alternating organic–inorganic perovskite and organic spacer layers; a prominent example of this structure (BA_2PbI_4) is shown in **Figure 1**a, with the butylammonium (BA^+) spacer ligand as used in this study. In RP perovskites, the organic spacer ligands are only anchored on the perovskite end; the other end of molecule is free to move and is mobile at room temperatures[26] for linear alkyl ligands. Since such motion may provide a mechanism for aiding diffusion of organic dopants within the organic layer, the central theme of our study is to exploit this structural feature to achieve bulk incorporation of molecular dopants.

For doping with molecular dopants, a series of 2D RP-perovskite films with chemical formulae of $BA_2MA_{n-1}Pb_nI_{3n+1}$ and 3D perovskite film with a chemical formula of methylammonium lead iodide ($MAPbI_3$) were spin-coated on Si substrates using precursors with different mixing ratios of butylammonium iodide (BAI), methylammonium iodide (MAI), and lead(II) iodide (PbI_2) (see Section S1, Supporting Information). While having the BA spacer layer as a common structural feature, the 2D RP perovskites consist of n layers of PbI_6 octahedra that can be tuned by varying the precursor stoichiometry. Structural and optical analyses including field-emission scanning electron microscope (FE-SEM; see Figure S1, Supporting Information), X-ray diffraction (XRD), and UV–vis absorbance spectra (see Figure S2a,b, Supporting Information) confirm the phase purity of these films with the desired stoichiometry.[4b,25a]

Screening of the potential dopants were initially attempted by spin-coating the toluene solutions of four widely employed molecular dopants: magic blue (denoted as MB, see Figure 1b), F_4TCNQ, BV, and cobaltocene. MB and F_4TCNQ are well-known p-type dopants,[19b,20,24] whereas BV and cobaltocene are common n-type dopants used in molecular electronics.[21,22] Figure S3 (Supporting Information) shows that out of these candidate dopants, MB consistently shows the largest increase in conductivity for the 2D RP perovskite series ($n = 1$–4); of note, MB and F_4TCNQ show negligible effects of doping since 3D perovskite ($MAPbI_3$) is known to be n-type due to iodide vacancies,[9,27] as confirmed later. Therefore, our focus was put on the MB dopant, including (1) conception of better doping protocols and (2) understanding the exact action of MB upon 2D RP perovskites.

Concerning the first point, one may immediately spot the shortcomings of doping protocol with spin-coating: the procedure is optimized for surface doping of films. Since the dopant solution is typically in a short contact with the film surface, the dopant molecules are not given sufficient time to diffuse into the bulk of film; this is in contrast with heteroatom doping in Si-based semiconductors in which the thermal diffusion of dopants allows the bulk of the Si lattice to be doped. While this is not an issue for 3D perovskites where diffusion of large molecular dopants into the bulk lattice is deemed difficult due to lack of available free spaces for molecular dopants, it offers sub-optimal condition for doping into 2D RP perovskites where the flexible and mobile organic ligands may offer spaces for these relatively voluminous molecules.[26] Therefore, a novel strategy similar to thermal diffusion in Si-doping was attempted by immersing the perovskite film in dopant solution for a given period of time (typically a few minutes). This method of doping, shown schematically in Figure 1c, is expected to allow ample time for dopants to diffuse into the bulk 2D structure, potentially using the grain
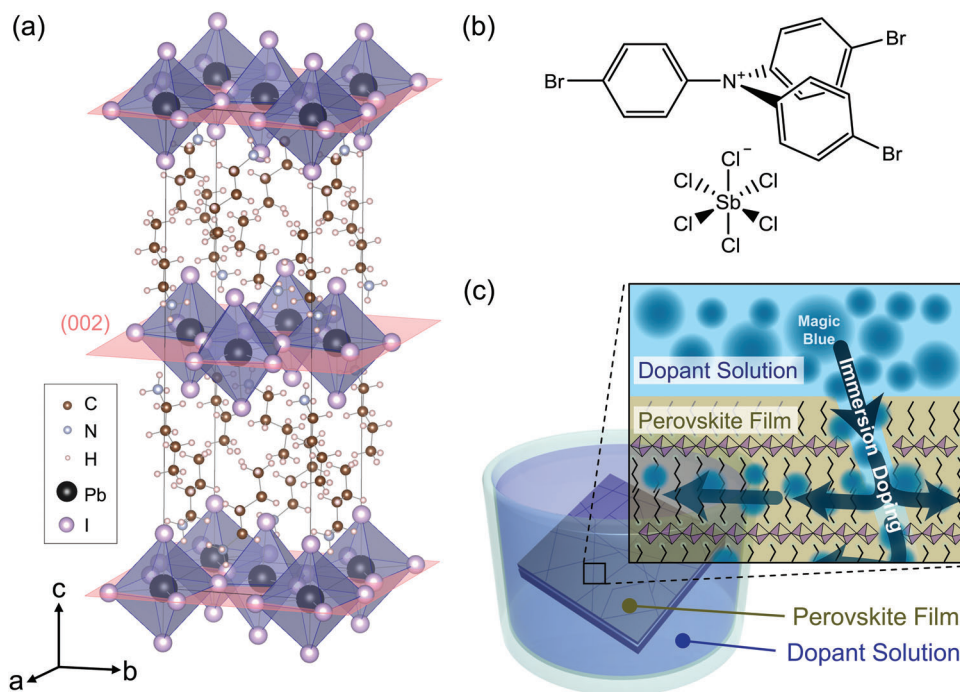
Figure 1. a) Crystal structure of BA_2PbI_4 ($n = 1$) perovskite used in this study. Highlighted is the (002) plane which gives rise to characteristic 6.4° reflection (see Figure 3a). b) Molecular structure of MB. c) Schematic illustration of immersion doping strategy used in this study. Cracks on wafer represents grain boundaries which allows dopant diffusion into the organic spacer layer.

boundaries as a channel for accessing the inner part of the film. As shown in the following section, this protocol results in a large increase in film conductivity, demonstrating the effectiveness of our immersion doping strategy.

2.2. Change of Electronic Properties upon MB Doping

The increase in current was confirmed with a current–voltage (I–V) characteristics of the doped films, the result of which is shown in **Figure 2**a (see Section S4, Supporting Information). The current in MB-immersion doped BA_2PbI_4 film increased by ≈60-fold relative to that of pristine film, with the prominent evolution of grain boundaries under optical microscopy (inset in Figure 2a) as expected from the proposed mechanism. Concurrent with this observation, atomic force microscopy examination on the BA_2PbI_4 film before and after doping showed a noticeable increase in values of R_q (a measure of film roughness, the square root of the sum of the squares of the individual heights and depths from the mean line), from 5.9 to 44.5 nm (see Figure S6, Supporting Information). Doped BA_2PbI_4 film also exhibits almost complete quenching of photoluminescence (PL) intensities (Figure 2b), which is expected from the increased probability of Auger recombination upon higher charge carrier densities.[28] In addition, while the excitonic peak absorption decreased according to UV–vis absorbance spectroscopy (see Figure 2c), the position of absorbance edge did not change upon doping, which verifies that the bandgap of the material is well maintained. The reduction in the excitonic peak may be related to the structural

change induced by the doping (discussed later) that might introduce some electronic disorder to the excitonic states.[29]

Ultraviolet photoelectron spectroscopy (UPS) results of doped film show an increase in the work function by 0.28 eV (Figure 2d), similar to the increase in the surface work function of doped film when measured with kelvin probe force microscopy (KPFM) (see Figure S7, Supporting Information). Hence, UPS and KPFM measurements corroborate that we have realized p-doping to the pristine BA_2PbI_4 ($n = 1$) perovskite.

Finally, we explore the effectiveness of MB-immersion doping on the film conductivity when the dimensionality n of the 2D perovskite layer is varied from $n = 1$ (BA_2PbI_4; most extreme 2D RP perovskite) to $n = \infty$ ($MAPbI_3$; 3D perovskite). The conductivity enhancement data presented in Figure 2e demonstrate a clear trend in decrease in the conductivity enhancement as the dimensionality shifts toward the 3D limit: while the $n = 1$ (BA_2PbI_4) film shows the maximum enhancement of ≈60, the figure drops to ≈20 ($n = 2$), ≈10 ($n = 3$), ≈2 ($n = 4$), and finally the conductivity even decreases upon doping for 3D $MAPbI_3$. UPS-measured Fermi levels of $n = 1$ 2D perovskite shows p-type tendency with Fermi level close to the valence band maximum (VBM), and 3D perovskite shows n-type tendency with Fermi level close to the conduction band minimum (CBM) (see Figure 2f). Since MB is known to be a p-dopant (LUMO level of magic blue: 5.5 eV),[24b] it seems that the doping with MB is most efficient in generating charge carriers when the Fermi level is close to VBM, as is the case for the $n = 1$ perovskite film (Fermi level of pristine $n = 1$ film : 4.02 eV).

However, we note that a part of the trend shown in the n versus conductivity enhancement plot (Figure 2e) can potentially

ADVANCED
SCIENCE NEWS
www.advancedsciencenews.com

ADVANCED
FUNCTIONAL
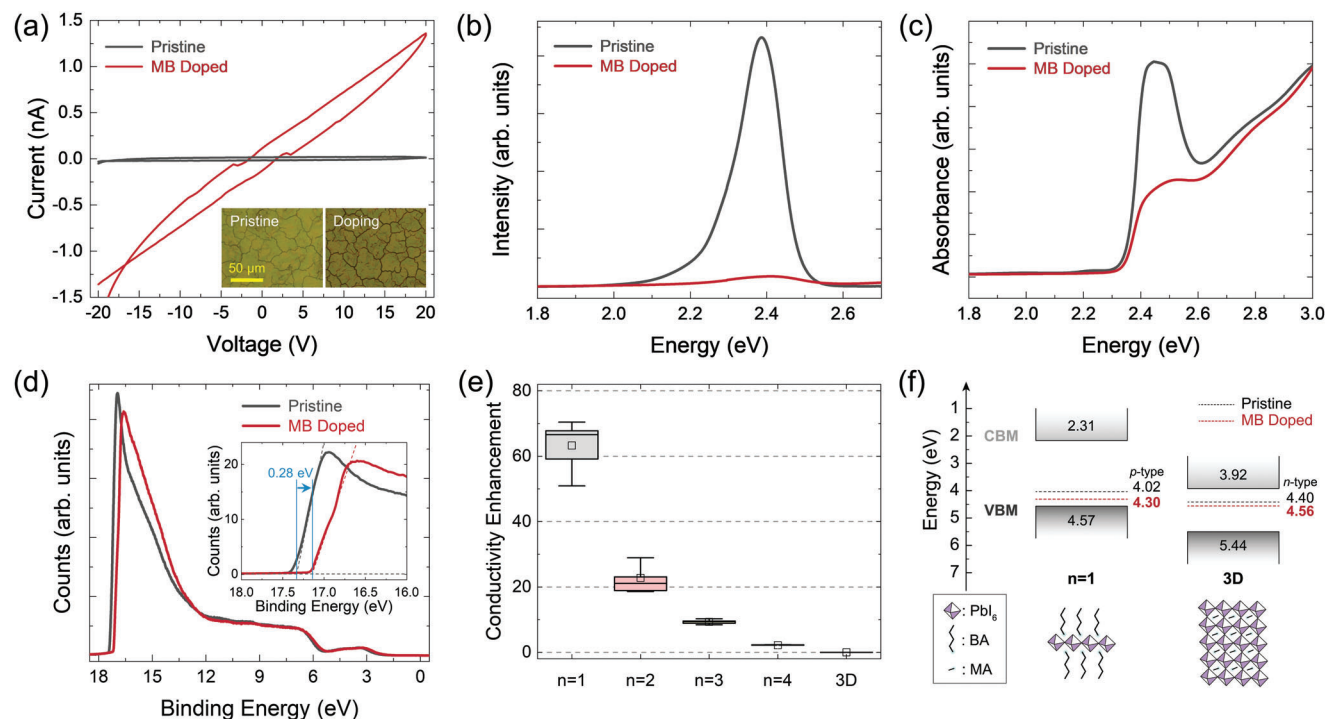**MATERIALS**
www.afm-journal.de

Figure 2. a) Current–voltage characteristics (inset; optical microscope images of the films), b) photoluminescence, c) UV–vis absorbance, and d) UPS data (inset; enlarged view near the secondary electron cutoff) of pristine and MB doped BA_2PbI_4 ($n = 1$) perovskites. e) Conductivity enhancement with MB doping for layered RP and 3D perovskites. f) Energy level diagram for RP and 3D perovskites shown in (e). Black and red dashed lines show the Fermi energy level of pristine and MB doped perovskites, respectively.

also arise from the decreasing proportion of organic ligand perovskite ratio upon increasing dimensionality: since the proposed mechanism of MB incorporation involves bulk penetration into organic spacer region, decrease in this ratio would allow smaller level of charge-transfer doping per given volume and thus gives only modest increases in conductivity. For 3D perovskites lacking any organic spacers, such bulk penetration is only available at the grain boundary surfaces and subsequently the smallest enhancement in conductivity is expected, which is in agreement with the experiment. Thus, both the band energies (electronic factor) and ratio of organic/perovskite layers (structural factor) need to be considered for bulk doping of 2D perovskites. For this reason, we will exclusively focus on MB immersion doping of the $n = 1$ BA_2PbI_4 perovskite, which gives the highest increase in electrical conductivity upon doping, from now on.

2.3. Structural and Electronic Changes upon Varying the Solvent

Another important factor other than the dopant material in immersion doping is the processing solvent. For effective doping of perovskite films, we note that the solvent should be able to dissolve MB to concentrations practical for doping while leaving the perovskite material intact. Initially, immersion doping was attempted by selecting a various range of solvents commonly utilized as anti-solvent for metal halide perovskites[5c,30] with the intention of minimizing the perovskite dissolution during immersion: chlorobenzene (CB), chloroform (CF), toluene (Tol), dichlorobenzene (DCB), and dichloromethane (DCM).

First, stability of $n = 1$ BA_2PbI_4 perovskite in each solvent was tested by simply immersing the spin-coated film in neat solvents for 2 h. The resulting changes to the film were checked with film XRD measurements, as the results are shown in **Figure 3**a (dashed lines). When compared to the pristine film ((002) reflection at 6.4° 2θ), CB, CF, Tol, and DCB did not register any significant changes apart from the appearance of a small shoulder to the low-angle region for CF and Tol, which can be regarded as a signature for elongated c-axis length per penetration of solvent molecules, albeit only to a small degree. This shoulder feature, however, is considerably enhanced for Tol and DCB upon using MB solutions rather than neat solvents (Figure 3a, solid lines): the shoulder at 6.1° 2θ dramatically grows in intensity especially for MB solution in DCB. While the reason for such improved penetration effect upon addition of MB is not yet clear, these XRD peak shifts indicate that dopant molecules can migrate into the bulk of perovskite film, therefore resulting in significant modulation of the c-axis length. In addition, the clear bimodal nature of (002) peak indicates that only a portion of perovskite domains, presumably those close to the film surface and/or grain boundaries, incorporates enough dopant/solvent molecules to show noticeable changes in XRD reflections; more discussion will follow on this heterogeneous spatial distribution.

The case of DCM needs special discussion since its behavior somewhat deviates from the other four solvents. When soaked in neat DCM, the (002) reflection shows an overall shift of −0.2° with substantial broadening that corresponds to ≈0.5 Å increase in the c-axis length. More importantly, the peak shape is now slightly skewed to the low-angle position; since this peak position
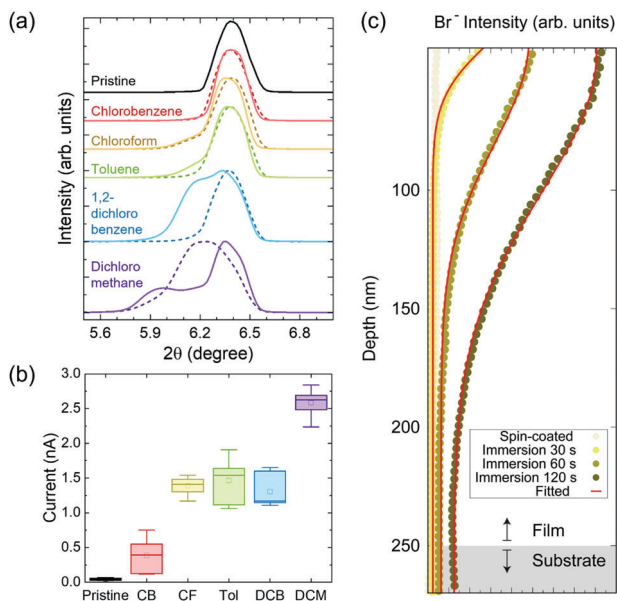
Figure 3. a) XRD data for BA_2PbI_4 ($n = 1$) films immersed in pure solvents (dashed lines) and MB solutions (solid lines). b) Maximum currents at 20 V applied voltages for BA_2PbI_4 ($n = 1$) films undoped (pristine) and doped with MB solutions employing various solvents. Legend: CB = chlorobenzene, CF = chloroform, Tol = toluene, DCB = 1,2-dichlorobenzene, DCM = dichloromethane. c) Br^- TOF-SIMS data of MB-doped BA_2PbI_4 ($n = 1$) film immersed in MB-toluene solution for different time durations. The data were fitted to a Fickian diffusion profile (see main text).

directly reflects the c-axis length, such skewed peak shape suggests a nonhomogeneous distribution of c-axis length that possibly arises from a gradient-like distribution of solvent molecules in the perovskite film. Such concentration gradient again can be present close to the film surface or around grain boundaries where the solvent molecules can access freely. Since the accessibility to perovskite structures must be shared between the solvent and dopant molecules (locations facile for solvents to approach must also be straightforward for dopants to access, and vice versa), the added dopant (MB) molecules are expected to preferably interact with the perovskite at locations with large solvent incorporation. Furthermore, since the solvent molecules are also capable of penetrating the organic spacer layer by themselves, the widening of spacer channels can also help the diffusion of dopants into the bulk of perovskite structure. The overall effect of this is a strong bimodal distribution of c-axis length and the (002) reflection, a result that is verified with XRD data (Figure 3a, purple solid line). The c-axis length in this case increases by ≈1.2 Å, which is on a similar order of magnitude to the thickness of tris(4-bromophenyl)ammonium cation in planar configuration normal to the c-axis. The effect of MB doping on conductivity is shown in Figure 3b. As expected from XRD, CB does not show any appreciable increase in current relative to that of the pristine film; all the other solvents exhibited current increases of 9.2–34.8 times, with DCM being the largest (61.2 times).

We also tracked the stability of doped structures by performing XRD measurements of immersion-doped films (in DCM solution) over a 15 day period. The films were stored under either

1) N_2 or 2) ambient conditions to evaluate their environmental stabilities. The resulting data in Figure S8 (Supporting Information) show the evolution of (002) reflection at 6.4° 2θ upon time. The small shoulder peak at 6.1° 2θ, which is characteristic of doped BA_2PbI_4 structure, does not show any appreciable change for the doped film stored in N_2, signifying the structural stability of doped phase. In contrast, storing the film in ambient air results in a gradual change in the structure with the shoulder peak gradually shifting toward the pristine (002) reflection, suggesting a gradual de-doping occurring in the perovskite structure.

As XRD measurements clearly showed signatures of heterogeneities in dopant distribution inside the perovskite film, spatial resolution of dopant locations along the normal axis of film was sought with time-of-flight secondary ion mass spectrometry (TOF-SIMS). Bromine was used as the probing element as a unique component in the organic (cation) part of MB (see Figure 1b). The resulting TOF-SIMS data in Figure 3c confirm the presence of Br^- ions originating from MB molecules in the bulk part of film buried several tens to hundreds of nm below the film surface. Increasing the immersion time from 30 sec to 2 min noticeably enhances both the dopant penetration depth (Br^- signals at deeper depths) and the level of dopant incorporation (Br^- signal intensity on TOF-SIMS). However, it was not possible to continuously increase the immersion time, because the quality of perovskite film degrades substantially when doping for a time exceeding 10 min (see Section S8, Supporting Information). While the film is stable under neat DCM for >2 h, adding MB into the solution seems to destabilize the perovskite structure and ends in significant damages in the film within a few minutes, possibly as a result of dopant penetration between the spacers. In contrast, dopant concentration seems to have little effect on the film surface: even when the doping concentration was varied 5 orders of magnitude from 0.01 to 100 mM, there was no observable damage to the crack on the film surface (see Figures S12–S14, Supporting Information). However, the appearance of grain boundaries with clear contrast on optical microscope images indicates preferential staining at these locations by MB solution, thus supporting our hypothesis of grain boundary-assisted diffusion of dopant molecules.

It is worth mentioning that the TOF-SIMS depth profiles of Br^- ion at varying immersion times are reminiscent of Fickian diffusion with a finite surface concentration of dopants, therefore signifying a surface-initiated diffusion (in direction normal to the film surface) occurring during the immersion period. The approximate length scale of such diffusion can be estimated by fitting the data to the following Fickian diffusion profile

$$I(x, t) = \frac{A_0}{\sqrt{\pi D t}} \exp\left(-\frac{x^2}{4Dt}\right) + C \tag{1}$$

where D is the diffusion coefficient, A_0 is the scaling factor, and C is the signal baseline. The resulting fits, which are shown in Figure 3c as solid red lines, yield diffusion constants of 8.6×10^{-14}, 1.7×10^{-13}, and 1.5×10^{-13} cm^2 s^{-1} for 30, 60 sec, and 2 min, respectively. These diffusion constants are all within the same order of magnitude, which suggests similar behavior of diffusion in action for all three samples as illustrated in Figure 1c. We also note that these values are several orders of magnitude lower than what was previously measured for various molecular dopants

**ADVANCED
SCIENCE NEWS**

www.advancedsciencenews.com

**ADVANCED
FUNCTIONAL
MATERIALS**

www.afm-journal.de

diffusing in semiconducting organic polymers: for example, diffusion constants of $\approx 10^{-10}$ and $\approx 10^{-6}$ cm^2 s^{-1} were observed for phenyl-C$_{61}$-butyric acid methyl ester (PCBM) in poly(3-hexylthiophene) (P3HT)[31] and F$_4$-TCNQ in P3HT,[32] respectively. In these cases, the lower crystallinity of polymer samples allows faster diffusion. However, diffusion of molecular dopants in bulk crystalline perovskites is expected to be more difficult (which contributes to the >4 orders of magnitude lower diffusion coefficients observed in our case) and thus optimizing the dopant/host combination will be needed to boost the dopant diffusivity and electrical conductivity.

2.4. Confirmation of Incorporation Doping through NMR

To further corroborate the bulk inclusion of dopant molecules through probing the structure after the doping process, solid-state NMR measurements were performed on the doped perovskite sample. Since solid-state NMR signals do not depend on the long-range structural ordering, detecting dopant molecules remaining after the charge transfer, as well as distinguishing the lead sites between the doped and pristine perovskite structures, is readily possible. We note that due to difficulties in preparing large quantities (>10 mg) of film samples to allow sufficient S/N for NMR spectroscopy, the samples were prepared through immersing the bulk BA$_2$PbI$_4$ powder in DCM solution of MB and filtering the resulting product. Powder XRD of this sample shows a similar shift in (002) reflection as the film sample, thus suggesting bulk incorporation of solvent and MB dopants (see Section S12, Supporting Information).

Molecular structure of tris(4-bromophenyl)amine, the reduction product after p-doping by MB dopant, is shown in **Figure 4**a. Structure of butylammonium cation (BA) is also given in Figure 4a, with each proton sites labeled in color. The two phenyl protons of tris(4-bromophenyl)amine, both labeled with olive, exhibit ^{1}H chemical shifts of 7.4 and 6.9 ppm in solution state, but are not clearly resolved in the solid-state spectrum (Figure S16, Supporting Information). The labeling scheme in color for each proton environment will be used consistently throughout the following results and discussion.

Figure 4a shows the ^{1}H NMR spectra of pristine and MB-doped BA$_2$PbI$_4$ samples. The spectrum of pristine sample (bottom) shows the expected peaks arising from only the BA molecules within the organic spacer layer (teal, –NH$_3^+$; dark grey, –CH$_2$; light grey, –CH$_3$ alkyl), which matches with our previous report on this phase.[26b] Upon doping with MB, one notices the appearance of a new peak at 6.8 ppm (shaded in olive); the ^{1}H shift of this peak is consistent with that of tris(4-bromophenyl)amine, indicating that the MB cation takes an electron from the perovskite structure, which results in a p-type doping. To prove this hypothesis, ^{207}Pb NMR experiments were subsequently performed on the perovskite samples before and after doping with MB. Since the local bonding environment of Pb should reflect such p-type doping of the perovskite lattice, one expects that the Pb atoms in MB-doped BA$_2$PbI$_4$ structure would show a different ^{207}Pb shift to that of pristine perovskites. The resulting ^{207}Pb spectra, shown in Figure 4b, clearly display the appearance of a new Pb peak at ≈ 920 ppm (shaded in brown), confirming the existence of new Pb environments after p-doping

with MB. We ascribe this new Pb environment to the change in electronic structure: the introduction of electron holes within the [PbI$_4$]$^{2-}$ perovskite layer likely induces a change in ^{207}Pb chemical shift, in a manner similar to ^{29}Si NMR peak shifts arising from doping in conventional Si semiconductors.[33] Quantification of ^{1}H MB peak in doped BA$_2$PbI$_4$ sample through a Lorentzian fitting shows that ≈ 0.09 MB molecule is incorporated per BA$_2$PbI$_4$ formula unit.

While ^{1}H and ^{207}Pb spectra unambiguously demonstrate successful p-doping of BA$_2$PbI$_4$ perovskites with MB, the 1D nature of spectra on Figure 4a,b with a single chemical shift axis does not allow to extract the precise position of MB dopants. This information could be extracted from 2D correlation spectroscopies (Figure 4c,d). These two spectra with independent ^{1}H/^{207}Pb (Figure 4c) and ^{1}H single-quantum/^{1}H double-quantum (Figure 4d) chemical shift axes on separate dimensions are capable of probing the spatial proximities between two nuclear spins, therefore specifying the location of dopant molecules in relation to the perovskite layers. To this end, two such correlation spectroscopic techniques are employed: ^{207}Pb–^{1}H heteronuclear correlation (HETCOR) and ^{1}H–^{1}H homonuclear correlation (back-to-back, or BABA). Whereas both experiments selectively detect two atomic spins in close proximities based on dipolar coupling, they provide complementary data in a sense that the former focusses on heteronuclear Pb–H correlation (i.e., between the perovskite layer and the organic dopant) while the latter looks at homonuclear H–H correlation (i.e., between the spacer layer and the organic dopant). Since NMR experiments are typically sensitive to signals originating from the bulk within the sample, the existence of such correlation is also a strong indication of bulk molecular doping, rather than surface doping as discussed in the Introduction.

The measured ^{207}Pb–^{1}H HETCOR spectrum is shown in Figure 4c. As the alternating layer-type crystal structure of n = 1 BA$_2$PbI$_4$ dictates molecular-level proximities between the BA molecule and the Pb atom, cross-peaks between the pristine (undoped) n = 1 ^{207}Pb peak (purple strip) and the BA ^{1}H environments (teal strip and grey strips) are clearly observed. At the same time, strong correlation between tris(4-bromophenyl)amine (olive) and doped n = 1 Pb site (brown) is evident; this correlation is an unequivocal evidence of dopant incorporation within the perovskite lattice, resulting in bulk doping of the perovskite structure. This analysis is also corroborated by ^{1}H–^{1}H BABA spectrum (Figure 4d), in which the correlation between tris(4-bromophenyl)amine (slanted olive strip) and all the BA environments suggests that the tris(4-bromophenyl)amine molecules reside within the BA organic spacer layers (Figure 4e).

2.5. Dopability Window and Rational Selection of Solvents for Immersion Doping

The analysis above demonstrates the importance of solvent for bulk incorporation of MB dopants in our immersion doping strategy. Since proper choice of solvent is crucial, one may wonder if a set of criteria for rational selection of solvents for efficient doping can be developed. We set the selection criteria based on the following basis: i) small solvent molecules, for effective penetration into the organic spacer layer; ii) good solubility of dopants
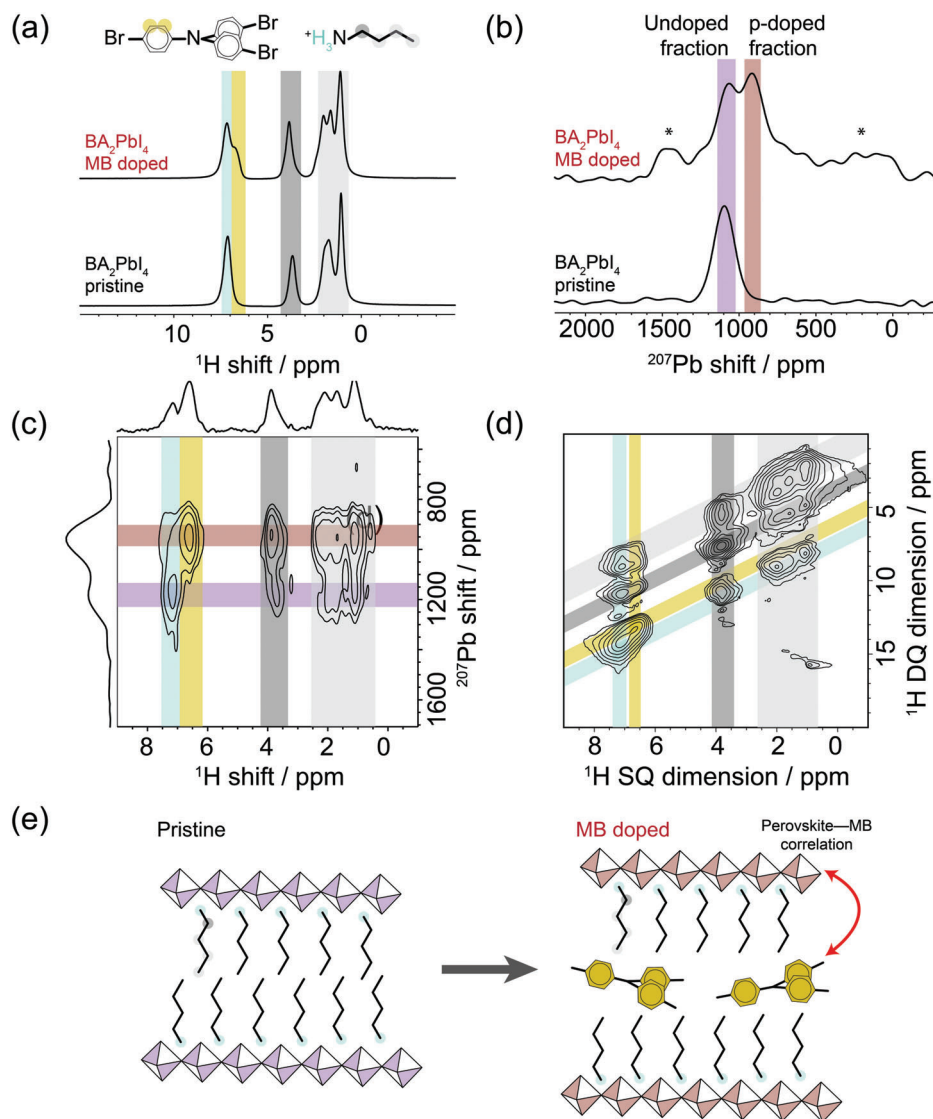
**ADVANCED
SCIENCE NEWS**
www.advancedsciencenews.com

**ADVANCED
FUNCTIONAL
MATERIALS**
www.afm-journal.de

Figure 4. a) Solid-state ^{1}H and b) ^{207}Pb Hahn-echo NMR spectra of pristine and MB-doped BA_2PbI_4 ($n = 1$) samples. Each proton and lead environments are color-labeled. c) ^{1}H–^{207}Pb HETCOR spectra of MB-doped BA_2PbI_4 ($n = 1$) sample, clearly showing the correlation of p-doped ^{207}Pb peak (brown) to aromatic MB ^{1}H peak (olive). d) ^{1}H DQ BABA spectra of MB-doped BA_2PbI_4 ($n = 1$) sample. e) Schematic scenario of inter-layer MB doping consistent with NMR and XRD data.

while being inert; iii) low to no dissolving power of perovskites; in addition, properties such as vapor pressure/boiling point (for efficient removal of solvents after immersion doping) and viscosity (diffusion of dopants in solution) may also be considered.

Although there are various methods of defining molecular sizes from a theoretical point of view such as Bader volumes,[34] the effective solvent size in our analysis was obtained by the formula below from known empirical solvent properties:

$$\text{effective solvent size} = \frac{10^{24}}{\frac{\rho}{M} N_A} \left(\text{Å}^3 \right) \quad (2)$$

where ρ is density (g mL^{-1}), M is molar mass (g mol^{-1}), N_A is Avogadro's number. The value of this size can be interpreted as the approximate van der Waals volume of each solvent molecule

in neat liquids. For the solubility, which is largely governed by the polarity of solvents, dielectric constant (ϵ_r) stands as a good metric for determining whether perovskite/dopant (both are polar in this case) would be soluble in polar/nonpolar solvents.

In order to systematically examine the factors that facilitate penetration of the dopant on the XRD spectra, multivariate analysis was used to analyze the characteristics of each solvent, such as solubility, vapor pressure, dipole moment, dielectric constant, and effective solvent size, as well as changes in XRD peak and conductivity as variables (Table S2, Supporting Information). Several correlations were found in the analysis process (see Figure S17, Supporting Information). Looking at the significant points, it was confirmed that there was a slight negative correlation between the dielectric constant and the change of the XRD peak, and there was a strong positive correlation between the effec-
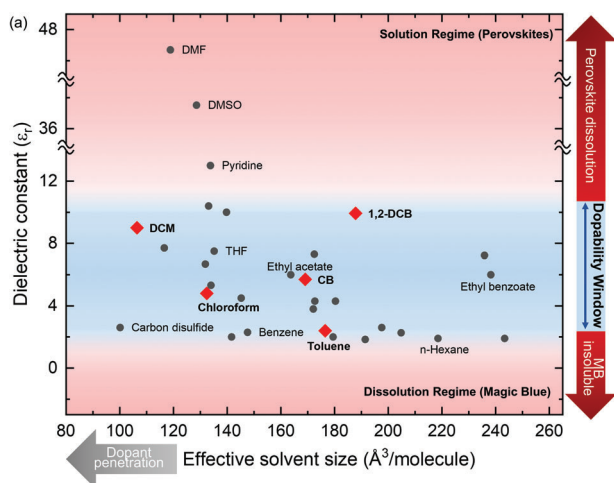
ADVANCED
SCIENCE NEWS

www.advancedsciencenews.com

ADVANCED
FUNCTIONAL
MATERIALS

www.afm-journal.de

Figure 5. Dielectric constant—solvent molecule size chart for solvent selection criteria in doping MB into RP perovskites. Several widely used solvents are labelled with text, with the ones tested in this study are highlighted with diamond symbols. Effective solvent size refers to the average van der Waals volume in Å obtained from solvent density (see text).

tive solvent size and the change in the XRD peak of the film immersed in the solvent or dopant solution. In particular, the change in current had a strong negative correlation between the position of the shoulder peak, which suggests that the change in electronic properties is commensurate with the dopant-induced changes in structural features (i.e., the amount of incorporated dopants).

Therefore, a group of widely used solvents were arranged with the effective solvent size which shows the greatest correlation with changes in XRD and the dielectric constant which is related to the dissolving properties of the dopant and the target perovskite, as two independent axes (**Figure 5**). Since both the perovskite and MB are polar, this puts a limit on the dielectric constants of usable solvents: if $\epsilon_r > 10$, perovskites simply dissolve in the solvent; if $\epsilon_r < 2$, polar MB is insoluble or poorly soluble. Hence, this effectively creates a window of dopability in terms of dielectric constant ϵ_r between 2 and 10. At the same time, as discussed above in relation to the XRD data, smaller solvent sizes will facilitate diffusion into the perovskite lattice. Thus, in our solvent selection chart (Figure 5), the best solvents should be located at the upper left corner of this dopability window. Multiple regression modeling of shoulder peak shift and conductivity scale against the effective solvent size and dielectric constant strongly supports this argument (see Figure S18, Supporting Information): within the dopability window, the smaller the effective solvent size and the larger the dielectric constant, the greater the shoulder peak shift effect and conductivity enhancement effect. In this regard, DCM stands out as the solvent of choice since it sits right within the dopability window with its small size, which is indeed the case seen in XRD and conductivity measurements.

2.6. Potentials for Improving the Immersion Doping Strategy

In this final section, we briefly discuss the current drawbacks of immersion doping and possible strategies to circumvent them. As alluded, the observed enhancement in the conductivity of over

60 times may seem small considering the preponderance of evidences presented in this work via the aforementioned various structural analyses. This likely arises from the surface-initiated bulk dopant incorporation, on a 100–200 nm scale along the depth of the film, as illustrated by the vertical TOF-SIMS data (Figure 3c). Thus, while doping of thicker (>200 nm) perovskite films may require different doping methodologies, the immersion doping recipe developed here can be easily adopted for perovskite films with thicknesses routinely used for (opto-)electronic devices.

Because perovskites have well-defined lattice structures, fundamental limit on the level of accessible doping may be obtained by considering the dopant geometries relative to the perovskite unit cell. Assuming a full (close-packed) incorporation of MB dopant into the organic spacer region and generation of single p^+ hole per MB molecule, $\approx 0.49\ p^+$ at maximum can be achieved per BA_2PbI_4 formula unit. Since quantification via ^1H NMR shows the presence of only 0.09 MB molecule in the doped samples, significant potential for further improving the doping methodology remains to be seen: this may involve changing the solvent/dopant combination and achieving a higher film stability under immersion for increasing the doping density. Especially, doping strategies to mitigate the appearance of cracks (as observed with staining, Figures S13 and S14, Supporting Information) need to be developed for obtaining better macroscale electrical conductivity in these samples, which again requires better understanding for the perovskite-solvent and perovskite-dopant interaction in these systems. In this aspect, the chemical framework of solvent selection criteria we presented in the current manuscript may serve as a starting point for further investigations. For instance, for doping of higher-order perovskites with $n>1$, we envisage that both the structural and electronic factors will influence the resulting enhancement in conductivities. As n increases, the ratio of the spacers to perovskite decreases, thus the amount of transferred positive charges per perovskite layer also decreases. Furthermore, the energy level mismatches of the magic blue dopant and perovskite film become worse for $n>1$ perovskites. Therefore, the size and energy level of dopants, as well as the relative solubilities of perovskites and dopants, have to be carefully evaluated to match the requirements of systems with different n. In this regard, our systematic approach of assessing the perovskite-dopant-solvent interaction can be straightforwardly extended to other combination of 2D perovskites and molecular dopants (F_4TCNQ, BV, etc.).

3. Conclusion

In this work, we demonstrated the possibility of doping 2D RP perovskites through bulk incorporation of molecular dopants. Perovskite films are kept immersed in dopant solution, during which dopants can penetrate into the bulk perovskite lattice with the action of solvent molecules modulating the organic spacer region. Combination of magic blue dopant and dichloromethane solvent in this immersion doping method achieves ≈ 60-fold enhancement in electrical conductivity for BA_2PbI_4 perovskite films, where bulk incorporation of dopant molecules is confirmed through XRD, NMR, and TOF-SIMS techniques. A rational design strategy for choosing the dopant/solvent pair is presented for the immersion doping method, which can be extended

to any 2D perovskite/molecular dopant pair for tuning the electrical properties of halide perovskite materials.

4. Experimental Section

Synthesis of Perovskite Precursor Solution: For BA_2PbI_4, the precursor solution was prepared by mixing 879.2 mg (4.37 mmol) of n-butylammonium iodide (BAI, 99%, Greatcellsolar) and 1008.0 mg (2.18 mmol) of lead(II) iodide (PbI_2, 99%, Sigma–Aldrich) in 1.802 mL N,N-dimethylformamide (DMF, 99.8%, Sigma–Aldrich) with 0.198 mL dimethyl sulfoxide (DMSO, ≥ 99.9%, Sigma–Aldrich), followed by stirring at 500 rpm at 50 °C for 6 h. For perovskite precursors of different dimensions, methylammonium iodide (MAI, ≥ 99.99%, Greatcellsolar) was used proportionally. See Table S1 (Supporting Information) for details.

Fabrication of Perovskite Film: SiO_2 (270 nm-thick) on Si and glass were used as substrates. The substrates were sequentially sonicated in acetone, 2-propanol, and deionized water for 10 min each. Then, the Si and glass substrates were cleaned using O_2 plasma treatment (200 mT, 30 sccm, 50 W) for 120 sec. After dropping 100 μL of precursor solution on the prepared substrate, the substrate was rotated at 500 rpm for 5 sec and then at 4000 rpm for 50 sec with a spin-coater, followed by drying in a nitrogen environment for 5 min and annealing at 100 °C for 10 min to fabricate each perovskite film.

Preparing Dopant Solution: Magic blue (408.25 mg (0.5 mmol)) (technical grade, Sigma-Aldrich) powder was dissolved in 50 mL of the solvent of interest (dichloromethane (DCM, ≥ 99.5%, Sigma–Aldrich), chloroform (CF, ≥ 99%, Sigma–Aldrich), chlorobenzene (CB, 99.8%, Sigma–Aldrich), dichlorobenzene (DCB, 99%, Sigma–Aldrich), and toluene (Tol, 99.8%, Sigma–Aldrich)), followed by stirring at 700 rpm for 20 min. As-dissolved solution was passed through a 4.5 μm PTFE filter (Whatman) to filter out the undissolved powder of the dopant solution.

Device Fabrication: After covering the prepared BA_2PbI_4 film with a shadow mask with a channel length of 50 μm and a width of 1 mm, an Au electrode with a thickness of 50 nm was deposited with an electron beam evaporator. Doping with dopant solution was performed by immersing the prepared film in the solution for 2 min. After taking out from the solution, the film was immediately spin-coated at 500 rpm for 5 sec and then at 4000 rpm for 50 sec, followed by drying in a nitrogen environment for 5 min.

Characterization and Measurement: *Scanning Electron Microscopy (SEM)*: The SEM images of the film were captured using JSM-7800F Prime at an acceleration voltage of 5–10 kV.

X-ray Diffraction (XRD): Crystallographic structures of perovskite films were measured by high-resolution X-ray diffraction (HRXRD) technique (Rigaku Smartlab).

Photoluminescence (PL) Spectroscopy: Steady-state PL spectra were analyzed by using a spectrofluorometer (JASCO FP-8500) with a 360 nm excitation source.

UV–vis Absorbance Spectroscopy: Absorbance spectra were measured using a UV–vis spectrophotometer (JASCO V-770) with an integrating sphere.

Atomic Force Microscopy (AFM): The surfaces of BA_2PbI_4 and doped films were characterized by an AFM system (Park Systems, NX-10 AFM).

Time-of-flight Secondary Ion Mass Spectrometer (TOF-SIMS): Depth profile information were obtained using the negative charge ionization polarity test method as a Cs^+, 1 keV, 100 nA etching source in ION-TOF, Germany TOF.SIMS 5.

Ultraviolet Photoelectron Spectroscopy (UPS) and X-ray Photoelectron Spectrometer (XPS): UPS and XPS spectra were analyzed in Kratos AXIS SUPRA.

Nuclear Magnetic Resonance (NMR): NMR measurements were performed with a 14.1 T Bruker Avance III spectrometer using a 1.3 mm Magic Angle Spinning (MAS) probe equipped at Seoul National University. Samples were packed into 1.3 mm zirconia rotor in an Ar-filled glovebox and were spun at 62.5 kHz. Rotor-synchronized ^1H and ^{207}Pb Hahn echo experiments were performed with radiofrequency (rf) pulse amplitudes of

200 and 175 kHz, respectively. Conditions for ^1H-detected $^{207}Pb \rightarrow ^1H$ experiments were optimized with ^{207}Pb rf amplitudes fixed to 100 kHz. Shifts were referenced to solid adamantane (^1H 1.87 ppm) and solid $Pb(NO_3)_2$ (^{207}Pb −3474 ppm).

Electrical Measurement: The *I–V* characteristics were measured using a semiconductor parameter analyzer (Keithley 4200 SCS). All the measurements were performed in a vacuum environment.

Supporting Information

Supporting Information is available from the Wiley Online Library or from the author.

Conflict of Interest

The authors declare no conflict of interest.

Data Availability Statement

The data that support the findings of this study are available from the corresponding author upon reasonable request.

[1] a) W. Nie, H. Tsai, R. Asadpour, J.-C. Blancon, A. J. Neukirch, G. Gupta, J. J. Crochet, M. Chhowalla, S. Tretiak, M. A. Alam, H.-L. Wang, A. D. Mohite, *Science* **2015**, *347*, 522; b) W. Yu, F. Li, L. Yu, M. R. Niazi, Y. Zou, D. Corzo, A. Basu, C. Ma, S. Dey, M. L. Tietze, U. Buttner, X. Wang, Z. Wang, M. N. Hedhili, C. Guo, T. Wu, A. Amassian, *Nat. Commun.* **2018**, *9*, 5354; c) T. Matsushima, S. Hwang, A. S. D. Sandanayaka, C. Qin, S. Terakawa, T. Fujihara, M. Yahiro, C. Adachi, *Adv. Mater.* **2016**, *28*, 10275.

[2] H. Huang, M. I. Bodnarchuk, S. V. Kershaw, M. V. Kovalenko, A. L. Rogach, *ACS Energy Lett.* **2017**, *2*, 2071.

[3] a) J. Euvrard, Y. Yan, D. B. Mitzi, *Nat. Rev. Mater.* **2021**, *6*, 531; b) S. Heo, K. Roh, F. Zhang, S. E. Tignor, A. B. Bocarsly, A. Kahn, B. P. Rand, *ACS Energy Lett.* **2022**, *7*, 211.

[4] a) B. Hwang, J.-S. Lee, *Adv. Opt. Mater.* **2019**, *7*, 1801356; b) J. C. Blancon, H. Tsai, W. Nie, C. C. Stoumpos, L. Pedesseau, C. Katan, M. Kepenekian, C. M. M. Soe, K. Appavoo, M. Y. Sfeir, S. Tretiak, P. M. Ajayan, M. G. Kanatzidis, J. Even, J. J. Crochet, A. D. Mohite, *Science* **2017**, *355*, 1288; c) Y. Fang, Q. Dong, Y. Shao, Y. Yuan, J. Huang, *Nat. Photon.* **2015**, *9*, 679; d) L. Dou, Y. Yang, J. You, Z. Hong, W.-H. Chang, G. Li, Y. Yang, *Nat. Commun.* **2014**, *5*, 5404.

[5] a) Z.-K. Tan, R. S. Moghaddam, M. L. Lai, P. Docampo, R. Higler, F. Deschler, M. Price, A. Sadhanala, L. M. Pazos, D. Credgington, F. Hanusch, T. Bein, R. H. Friend, *Nat. Nanotechnol.* **2014**, *9*, 687; b) X. Zhao, Z.-K. Tan, *Nat. Photon.* **2020**, *14*, 215; c) H. Cho, S.-H. Jeong, M.-H. Park, Y.-H. Kim, C. Wolf, C.-L. Lee, J. H. Heo, A. Sadhanala, N. Myoung, S. Yoo, S. H. Im, R. H. Friend, T.-W. Lee, *Science* **2015**, *350*, 1222; d) Y. Cao, N. Wang, H. Tian, J. Guo, Y. Wei, H. Chen, Y. Miao, W. Zou, K. Pan, Y. He, H. Cao, Y. Ke, M. Xu, Y. Wang, M. Yang, K. Du, Z. Fu, D. Kong, D. Dai, Y. Jin, G. Li, H. Li, Q. Peng, J. Wang, W. Huang, *Nature* **2018**, *562*, 249.

[6] a) H. Choi, C.-K. Mai, H.-B. Kim, J. Jeong, S. Song, G. C. Bazan, J. Y. Kim, A. J. Heeger, *Nat. Commun.* **2015**, *6*, 7348; b) H. Tsai, W. Nie, J.-C. Blancon, C. C. Stoumpos, R. Asadpour, B. Harutyunyan, A. J. Neukirch, R. Verduzco, J. J. Crochet, S. Tretiak, L. Pedesseau, J. Even, M. A. Alam, G. Gupta, J. Lou, P. M. Ajayan, M. J. Bedzyk, M. G. Kanatzidis, A. D. Mohite, *Nature* **2016**, *536*, 312; c) M. Kim, G.-H. Kim, T. K. Lee, I. W. Choi, H. W. Choi, Y. Jo, Y. J. Yoon, J. W. Kim, J. Lee, D. Huh, H. Lee, S. K. Kwak, J. Y. Kim, D. S. Kim, *Joule* **2019**, *3*, 2179; d) J. M. Frost, K. T. Butler, F. Brivio, C. H. Hendon, M. van Schilfgaarde, A. Walsh, *Nano Lett.* **2014**, *14*, 2584; e) M. A. Green, A. Ho-Baillie, H. J. Snaith, *Nat. Photon.* **2014**, *8*, 506; f) J. M. Frost, A. Walsh, *Acc. Chem. Res.* **2016**, *49*, 1500963; g) T. Leijtens, G. E. Eperon, N. K. Noel, S. N. Habisreutinger, A. Petrozza, H. J. Snaith, *Adv. Energy Mater.* **2015**, *5*, 1500963.

[7] a) H. Zhu, A. Liu, K. I. Shim, J. Hong, J. W. Han, Y.-Y. Noh, *Adv. Mater.* **2020**, *32*, 2002717; b) A. Liu, H. Zhu, S. Bai, Y. Reo, T. Zou, M.-G. Kim, Y.-Y. Noh, *Nat. Electron.* **2022**, *5*, 78; c) X.-J. She, C. Chen, G. Divitini, B. Zhao, Y. Li, J. Wang, J. F. Orri, L. Cui, W. Xu, J. Peng, S. Wang, A. Sadhanala, H. Sirringhaus, *Nat. Electron.* **2020**, *3*, 694; d) S. P. Senanayak, M. Abdi-Jalebi, V. S. Kamboj, R. Carey, R. Shivanna, T. Tian, G. Schweicher, J. Wang, N. Giesbrecht, D. Di Nuzzo, H. E. Beere, P. Docampo, D. A. Ritchie, D. Fairen-Jimenez, R. H. Friend, H. Sirringhaus, *Sci. Adv.* **2020**, *6*, eaaz4948; e) S. P. Senanayak, B. Yang, T. H. Thomas, N. Giesbrecht, W. Huang, E. Gann, B. Nair, K. Goedel, S. Guha, X. Moya, C. R. McNeill, P. Docampo, A. Sadhanala, R. H. Friend, H. Sirringhaus, *Sci. Adv.* **2017**, *3*, e1601935.

[8] a) K. Kang, H. Ahn, Y. Song, W. Lee, J. Kim, Y. Kim, D. Yoo, T. Lee, *Adv. Mater.* **2019**, *31*, 1804841; b) B. Hwang, J.-S. Lee, *Sci. Rep.* **2017**, *7*, 673.

[9] Q. Wang, Y. Shao, H. Xie, L. Lyu, X. Liu, Y. Gao, J. Huang, *Appl. Phys. Lett.* **2014**, *105*, 163508.

[10] a) Z. Tang, T. Bessho, F. Awai, T. Kinoshita, M. M. Maitani, R. Jono, T. N. Murakami, H. Wang, T. Kubo, S. Uchida, H. Segawa, *Sci. Rep.* **2017**, *7*, 12183; b) M. Abdi-Jalebi, Z. Andaji-Garmaroudi, S. Cacovich, C. Stavrakas, B. Philippe, J. M. Richter, M. Alsari, E. P. Booker, E. M. Hutter, A. J. Pearson, S. Lilliu, T. J. Savenije, H. Rensmo, G. Divitini, C. Ducati, R. H. Friend, S. D. Stranks, *Nature* **2018**, *555*, 497.

[11] a) J. Yang, S. C. Cho, S. Lee, J. W. Yoon, W. H. Jeong, H. Song, J. T. Oh, S. G. Lim, S. Y. Bae, B. R. Lee, M. Ahmadi, E. H. Sargent, W. Yi, S. U. Lee, H. Choi, *ACS Nano* **2022**, *16*, 1649; b) W. H. Jeong, Z. Yu, L. Gregori, J. Yang, S. R. Ha, J. W. Jang, H. Song, J. H. Park, E. D. Jung, M. H. Song, S. H. Park, H. J. Snaith, A. Boretti, F. De Angelis, D. Meggiolaro, J. Lee, H. Choi, B. R. Lee, *J. Mater. Chem. A* **2021**, *9*, 26750; c) Z. Yu, W. H. Jeong, K. Kang, H. Song, X. Shen, H. Ahn, S. W. Lee, X. Fan, J. W. Jang, S. R. Ha, J. W. Min, J. H. Park, J. Han, E. D. Jung, M. H. Song, D. W. Chang, W. B. Im, S. H. Park, H. Choi, B. R. Lee, *J. Mater. Chem. A* **2022**, *10*, 13928.

[12] W. Tress, J. P. Correa Baena, M. Saliba, A. Abate, M. Graetzel, *Adv. Energy Mater.* **2016**, *6*, 1600396.

[13] L. Huang, S. Bu, D. Zhang, R. Peng, Q. Wei, Z. Ge, J. Zhang, *Sol. RRL* **2019**, *3*, 1800274.

[14] A. L. Abdelhady, M. I. Saidaminov, B. Murali, V. Adinolfi, O. Voznyy, K. Katsiev, E. Alarousu, R. Comin, I. Dursun, L. Sinatra, E. H. Sargent, O. F. Mohammed, O. M. Bakr, *J. Phys. Chem. Lett.* **2016**, *7*, 295.

[15] Z. Fang, L. He, H. Gan, L. Ji, Z. Ye, *Advanced Science* **2018**, *5*, 1800736.

[16] Q. Chen, L. Chen, F. Ye, T. Zhao, F. Tang, A. Rajagopal, Z. Jiang, S. Jiang, A. K. Y. Jen, Y. Xie, J. Cai, L. Chen, *Nano Lett.* **2017**, *17*, 3231.

[17] M. Abdi-Jalebi, M. Pazoki, B. Philippe, M. I. Dar, A. Sadhanala, G. Divitini, R. Imani, S. Lilliu, J. Kullgren, H. Rensmo, M. Grätzel, R. H. Friend, *ACS Nano* **2018**, *12*, 7301.

[18] W. Travis, E. N. K. Glover, H. Bronstein, D. O. Scanlon, R. G. Palgrave, *Chem. Sci.* **2016**, *7*, 4548.

[19] a) K. Kang, S. Watanabe, K. Broch, A. Sepe, A. Brown, I. Nasrallah, M. Nikolka, Z. Fei, M. Heeney, D. Matsumoto, K. Marumoto, H. Tanaka, S.-i. Kuroda, H. Sirringhaus, *Nat. Mater.* **2016**, *15*, 896; b) Y. Kim, S. Chung, K. Cho, D. Harkin, W.-T. Hwang, D. Yoo, J.-K. Kim, W. Lee, Y. Song, H. Ahn, Y. Hong, H. Sirringhaus, K. Kang, T. Lee, *Adv. Mater.* **2019**, *31*, 1806697; c) Y. Kim, K. Broch, W. Lee, H. Ahn, J. Lee, D. Yoo, J. Kim, S. Chung, H. Sirringhaus, K. Kang, T. Lee, *Adv. Funct. Mater.* **2020**, *30*, 2000058; d) K. Kang, S. Schott, D. Venkateshvaran, K. Broch, G. Schweicher, D. Harkin, C. Jellett, C. B. Nielsen, I. McCulloch, H. Sirringhaus, *Mater. Today Phys.* **2019**, *8*, 112.

[20] E. A. Gaulding, J. Hao, H. S. Kang, E. M. Miller, S. N. Habisreutinger, Q. Zhao, A. Hazarika, P. C. Sercel, J. M. Luther, J. L. Blackburn, *Adv. Mater.* **2019**, *31*, 1902250.

[21] a) D. Kiriya, M. Tosun, P. Zhao, J. S. Kang, A. Javey, *J. Am. Chem. Soc.* **2014**, *136*, 7853; b) J. Jang, J.-K. Kim, J. Shin, J. Kim, K.-Y. Baek, J. Park, S. Park, Y. D. Kim, S. S. P. Parkin, K. Kang, K. Cho, T. Lee, *Sci. Adv.* **2022**, *8*, eabn3181.

[22] a) C. K. Chan, F. Amy, Q. Zhang, S. Barlow, S. Marder, A. Kahn, *Chem. Phys. Lett.* **2006**, *431*, 67; b) E. E. Perry, J. G. Labram, N. R. Venkatesan, H. Nakayama, M. L. Chabinyc, *Adv. Electron. Mater.* **2018**, *4*, 1800087.

[23] a) D. Ricciarelli, D. Meggiolaro, F. Ambrosio, F. De Angelis, *ACS Energy Lett.* **2020**, *5*, 2787; b) T. Sheikh, V. Nawale, N. Pathoor, C. Phadnis, A. Chowdhury, A. Nag, *Angew. Chem., Int. Ed.* **2020**, *59*, 11653.

[24] a) A. I. Hofmann, R. Kroon, S. Zokaei, E. Järsvall, C. Malacrida, S. Ludwigs, T. Biskup, C. Müller, *Adv. Electron. Mater.* **2020**, *6*, 2000249; b) J.-K. Kim, K. Cho, J. Jang, K.-Y. Baek, J. Kim, J. Seo, M. Song, J. Shin, J. Kim, S. S. P. Parkin, J.-H. Lee, K. Kang, T. Lee, *Adv. Mater.* **2021**, *33*, 2101598.

[25] a) D. H. Cao, C. C. Stoumpos, O. K. Farha, J. T. Hupp, M. G. Kanatzidis, *J. Am. Chem. Soc.* **2015**, *137*, 7843; b) C. C. Stoumpos, D. H. Cao, D. J. Clark, J. Young, J. M. Rondinelli, J. I. Jang, J. T. Hupp, M. G. Kanatzidis, *Chem. Mater.* **2016**, *28*, 2852; c) C. M. M. Soe, G. P. Nagabhushana, R. Shivaramaiah, H. Tsai, W. Nie, J.-C. Blancon, F. Melkonyan, D. H. Cao, B. Traoré, L. Pedesseau, M. Kepenekian, C. Katan, J. Even, T. J. Marks, A. Navrotsky, A. D. Mohite, C. C. Stoumpos, M. G. Kanatzidis, *Proc. Natl. Acad. Sci. USA* **2019**, *116*, 58.

[26] a) C. J. Dahlman, R. M. Kennard, P. Paluch, N. R. Venkatesan, M. L. Chabinyc, G. N. M. Reddy, *Chem. Mater.* **2021**, *33*, 642; b) J. Lee, W. Lee, K. Kang, T. Lee, S. K. Lee, *Chem. Mater.* **2021**, *33*, 370.

[27] A. Zohar, N. Kedem, I. Levine, D. Zohar, A. Vilan, D. Ehre, G. Hodes, D. Cahen, *J. Phys. Chem. Lett.* **2016**, *7*, 191.

[28] Y. Jiang, M. Cui, S. Li, C. Sun, Y. Huang, J. Wei, L. Zhang, M. Lv, C. Qin, Y. Liu, M. Yuan, *Nat. Commun.* **2021**, *12*, 336.

[29] a) M. D. Smith, L. Pedesseau, M. Kepenekian, I. C. Smith, C. Katan, J. Even, H. I. Karunadasa, *Chem. Sci.* **2017**, *8*, 1960; b) W. Zhou, D. Li, D. Zhang, H. Tang, H. Zhang, C. Liang, *RSC Adv.* **2019**, *9*, 14718; c) M. Baranowski, P. Plochocka, *Adv. Energy Mater.* **2020**, *10*, 1903659; d) B. Cheng, T.-Y. Li, P. Maity, P.-C. Wei, D. Nordlund, K.-T. Ho, D.-H.

**ADVANCED
SCIENCE NEWS**

www.advancedsciencenews.com

**ADVANCED
FUNCTIONAL
MATERIALS**

www.afm-journal.de

Lien, C.-H. Lin, R.-Z. Liang, X. Miao, I. A. Ajia, J. Yin, D. Sokaras, A. Javey, I. S. Roqan, O. F. Mohammed, J.-H. He, *Commun. Phys.* **2018**, *1*, 80; e) D. Marongiu, M. Saba, F. Quochi, A. Mura, G. Bongiovanni, *J. Mater. Chem. C* **2019**, *7*, 12006.

[30] M. Xiao, F. Huang, W. Huang, Y. Dkhissi, Y. Zhu, J. Etheridge, A. Gray-Weale, U. Bach, Y.-B. Cheng, L. Spiccia, *Angew. Chem., Int. Ed.* **2014**, *53*, 9898.

[31] B. Watts, W. J. Belcher, L. Thomsen, H. Ade, P. C. Dastoor, *Macromolecules* **2009**, *42*, 8392.

[32] J. Li, C. Koshnick, S. O. Diallo, S. Ackling, D. M. Huang, I. E. Jacobs, T. F. Harrelson, K. Hong, G. Zhang, J. Beckett, M. Mascal, A. J. Moulé, *Macromolecules* **2017**, *50*, 5476.

[33] E. M. Meintjes, W. W. Warren, J. P. Yesinowski, *Solid State Nucl. Magn. Reson.* **2013**, *55–56*, 91.

[34] a) R. F. W. Bader, in *Atoms in Molecules : A Quantum Theory*, Clarendon press, Oxford, UK **1990**; b) W. Tang, E. Sanville, G. Henkelman, *J. Phys.: Condens. Matter* **2009**, *21*, 084204.